Applied Mathematical Modelling 92 (2021) 546–564

Contents lists available at ScienceDirect

Applied Mathematical Modelling

journal homepage: www.elsevier.com/locate/apm

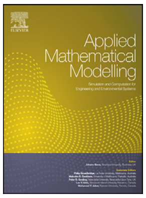

A semianalytical Hertzian frictional contact model in 2D

Zhengshou Lai[a], Qiushi Chen[b], Linchong Huang[c,*]

[a] *School of Intelligent Systems Engineering, Sun Yat-sen University, Shenzhen 518107, China*
[b] *Glenn Department of Civil Engineering, Clemson University, Clemson, SC 29634, USA*
[c] *School of Aeronautics and Astronautics Engineering, Sun Yat-sen University, Shenzhen 518107, China*

ARTICLE INFO

Article history:
Received 21 April 2020
Revised 24 October 2020
Accepted 8 November 2020
Available online 18 November 2020

Keywords:
Hertzian contact stress
Frictional contact model
Discrete element method
Two-dimensional
Parallel-axis cylinders

ABSTRACT

The Hertzian contact model is prominent for characterizing the contact behaviors of particles in three dimensions (3D), while its two-dimensional (2D) version in the tangential direction has not been well-established yet. In this work, a semianalytical Hertzian frictional contact model in 2D is developed, with an analytical solution for the normal contact behavior and a semianalytical solution with a variable penalty factor for the tangential contact behavior. Numerical analyses with finite element simulations are performed to characterize the penalty factor and validate the proposed contact model. The results show that the penalty factor increases with the contact width and Poisson's ratio based on which an empirical equation of the penalty factor is provided. Using the penalty factor calculated from the empirical equation, the contact behaviors evaluated from the proposed contact model match fairly well with those of finite element simulations. The proposed contact model is implemented in a discrete element code. Quantitative analyses of a bi-axial compression test on polydispersed particles demonstrate the stability and effectiveness of the proposed contact model. The proposed contact model could be useful to the computational mechanics of particles in 2D and parallel-axis cylinders with strip contacts in 3D.

1. Introduction

Discrete element method (DEM) refers to a class of computational models that are widely used to model the mechanical behaviors of particulate systems. The method was originally introduced by Cundall and Strack [1] for geomaterials, and has since been applied and gained tremendous popularity in various engineering disciplines (e.g., [2–8]) to study particulate systems. In DEM, every particle is explicitly modeled in the Lagrangian framework using particle models, with the interactions between particles described by contact models and the motion and kinematics of particles governed by the Newton-Euler equations [9,10]. The mechanical behavior of a particulate system is then presented as an assembly of the translations and rotations of all the constituent particles. A key component of DEM is the contact models, which characterize the relationship between the interactive forces and relative displacements of the particles in contact. The fidelity of a DEM modeling relies upon the accuracy of the adopted contact models.

Over the years, many contact models have been postulated (e.g., [1,11–16]), whereas two of the most commonly used ones (considering only the normal and tangential interactions) are the linear spring model [1] and the nonlinear Hertzian model [11–13]. The linear spring model considers the interactions between colliding particles as linear springs [17]. It is

---

[*] Corresponding author.
E-mail addresses: hlinch@mail.sysu.edu.cn, huanglinchong@126.com (L. Huang).

https://doi.org/10.1016/j.apm.2020.11.016

simple in implementation and computationally efficient and thus has been adopted in many DEM studies (e.g., [4,18–20]). With proper calibration of the contact stiffness [21,22], the linear spring model is able to qualitatively resemble both the microscopic and macroscopic mechanical behaviors of particulate systems [17,23,24]. However, the linear spring model has the disadvantages that (1) it oversimplifies the force-displacement relationship and (2) the contact stiffness lacks physical meaning and is difficult to quantify from laboratory experiments [18,25]. On the other hand, the nonlinear Hertzian model explicitly considers the traction and compliance at the contact surface [26]. It can accurately capture the nonlinear force-displacement behaviors of particle contacts [27], and in addition to that, the contact stiffness has a direct correlation with the common mechanical properties such as Young's modulus and Poisson's ratio. In this respect, the nonlinear Hertzian model is more attractive than the linear spring model for the DEM simulations of high fidelity.

The core of the Hertzian contact model is the Hertzian contact stresses, which refers to the localized stresses that develop in particles as the particle surfaces come in contact and deform slightly under imposed loads [11,12]. The stress and strain distributions in the colliding particles are first characterized based on the Hertz's theory, and then the force-displacement relationships are found by integrating the stresses and strains. However, to characterize the stress and strain distributions in the colliding particles is not a trivial task, as the stresses and strains are heavily dependent on the shapes of the particles. In fact, solutions for the Hertzian contact stress-based contact behaviors are limited to a class of simple geometries, such as spheres (i.e., the famous Hertz-Mindlin solution [11,12,28]). For particles with non-spherical shapes, the Hertz-Mindlin solution is often adopted to obtain an approximation of the contact behaviors by using spherical particles of same surface curvature at the contact [12,24,29]. With this treatment, the Hertzian-Mindlin solution is available and has become a prominent model to characterize the contact behaviors of particles in three dimensions (3D).

A special case of particle contacts in 3D is the contacts between cylinders that are pressed together with their axes aligned and subject to transverse shearing forces. Some examples of such a case can be seen in wheel-rail or tire-street contacts, roll bearings, gears, fuel rods and et al. They can be as well simplified as contacts in 2D by plane strain assumption. The contact between parallel-axis cylinders is a rectangle strip with slip and slide regions, the boundaries of which are dependent on the magnitudes of the normal and tangential forces. The stress distributions in the contact between parallel-axis cylinders were first studied by Cattaneo [30] and Mindlin [28], and their solution was later summarized in Johnson [12]. The results were later extended by Kim et al. [31] with the consideration of the effects of sequentially applied shearing forces in perpendicular directions. A common limitation of these works is that the effects of friction in the contact zone and the influence of shear stress on the normal stress in contact were neglected. In this regard, Zhupanska and Ulitko [32] developed an exact solution to the problem of indentation with friction of a rigid cylinder into an elastic half-space using the the Wiener-Hopf technique. Recently, Klimchuk and Ostryk [33] studied the stress distributions inside colliding particles, and investigated the effects of friction on the formation of adhesion zone in the contact area and distribution of maximum tangential stress within the cylinders. From the experiment perspective, Burguete and Patterson [34] conducted a photoelastic study of the contact between a cylinder and a half-space. The stress distributions in the cylinder were obtained and compared with the theoretical and numerical models of this type of contact. It should be pointed out that these aforementioned studies put an emphasis on the stress distributions in the contact whereas the contact deformations were less explored. In Johnson [12], it was stated that for Hertzian distribution of normal or tangential pressure, the surface displacements in the cylinders are distributed parabolically within the contact strip. Based on the approach of strain integration, solutions for the force-displacement relationship of contact of cylinders in the normal direction were developed in Johnson [12], Pereira et al. [25], 35], while the force-displacement relationship in the tangential direction, particularly with the consideration of micro slip effects, is still not well established.

This work aims to establish a physics-based Hertzian frictional contact model for the computational contact mechanics in 2D. To begin with, the deformation of an elastic half-space subjected to Hertzian distributed tractions is analyzed. Then, following a strategy similar to the Johnson's solution [12], the normal force-displacement relationship for 2D round bodies is revisited, and a semianalytical solution with a variable penalty factor is proposed for the tangential force-displacement relationship. After that, the Hertzian frictional contact model in 2D is developed by combining the normal and tangential force-displacement behaviors of the two particles in contact with special consideration of the full slip or partial slip conditions of the contact. Considering the effects of loading history, the simplification and implementation of the proposed contact model in DEM are also discussed. Finally, numerical sub-particle analyses with finite element simulations are performed to characterize the penalty factor and validate the proposed contact model. In addition, a DEM simulation of the bi-axial compression test on polydispersed particles is presented to further demonstrate the performance of the proposed contact model.

2. Preliminaries

2.1. Hertz's theory of elastic contact

Considering two round particles shown in Fig. 1, a normal force gives rise to a contact plane. In this work, the discussion is limited to non-conformal contacts, in which particles only touch at one point (or along a line in 3D) at the onset of contact [36]. Another distinct type of contact is the conformal contacts, in which particles touch at multiple points before any contact deformation takes place [37]. The non-conformal contacts are the common ones in DEM. For a non-conformal contact, the contact area is small compared to the particle sizes, and the stresses are highly concentrated in the contact

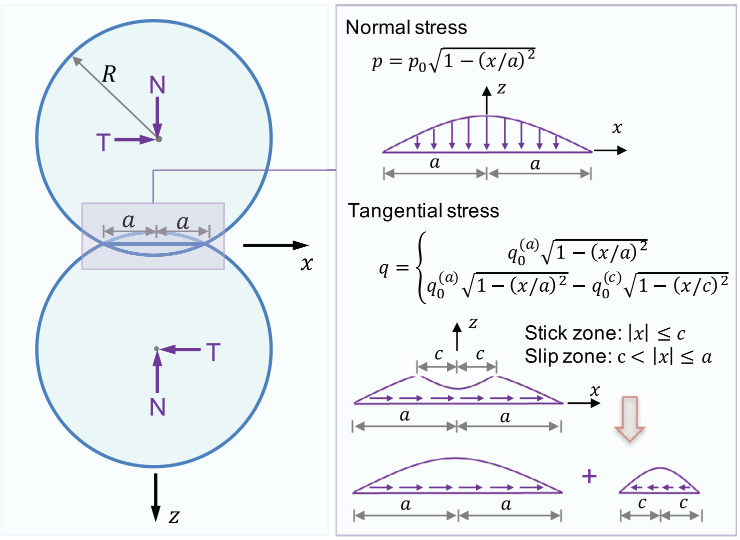

Fig. 1. Illustrative diagram of the contact between two round particles.

area. According to the Hertz's theory [11,12,38], the normal stress p in the contact can be approximately characterized by an elliptical equation, and the tangential stress q is a combination of two elliptical equations, such that

$$p = \frac{2N}{\pi a}\left(1 - x^2/a^2\right)^{1/2}, \quad |x| \leq a \tag{1}$$

$$q = \begin{cases} \frac{2\mu N}{\pi a}\left(1 - x^2/a^2\right)^{1/2}, & c < |x| \leq a \\ \frac{2\mu N}{\pi a}\left(1 - x^2/a^2\right)^{1/2} - \frac{2\left(c^2/a^2\right)\mu N}{\pi c}\left(1 - x^2/c^2\right)^{1/2}, & |x| \leq c \end{cases} \tag{2}$$

where N is the total normal contact force integrated from the normal contact stress, μ is the contact friction coefficient, a is the half-width of the contact plane, and c is the half-width of the stick zone within the contact. It should be noted that in Eq. (2), the Coulomb's law of friction [12,39] has been implicitly incorporated. The total tangential contact force T can be obtained by integrating the tangential contact stresses, which gives

$$T = \mu N(1 - c^2/a^2) \tag{3}$$

The contact half-width can be related to the normal contact force through

$$a = \left(\frac{4NR^\star}{\pi E^\star}\right)^{1/2} \tag{4}$$

where $E^\star$ and $R^\star$ are the composite modulus and composite radius, respectively, which are defined as

$$\frac{1}{E^\star} = \frac{1-\nu_1^2}{E_1} + \frac{1-\nu_2^2}{E_2} \tag{5}$$

$$\frac{1}{R^\star} = \frac{1}{R_1} + \frac{1}{R_2} \tag{6}$$

where ν and E are the Poisson's ratio and Young's modulus, respectively; R is the particle radius; and the subscripts 1 and 2 indicate the associated particle index. By substituting Eq. (4) into Eq. (3) and rearranging terms, the half-width of the stick zone can be related to the contact forces through

$$c = \left(1 - \frac{T}{\mu N}\right)\left(\frac{4NR^\star}{\pi E^\star}\right)^{1/2} \tag{7}$$

2.2. Hertzian distributed loading on a half-space

This section analyzes the deformation of an elastic half-space subjected to Hertzian distributed loading. The deformation of the half-space due to concentrated normal and tangential forces is first studied, and then the deformation due to Hertzian distributed tractions is obtained by integration. Fig. 2 shows the cross-section of a half-space. In this frame, the boundary surface is the x-axis, and the z-axis is directed into the solid. The lateral and bottom boundaries are fixed with

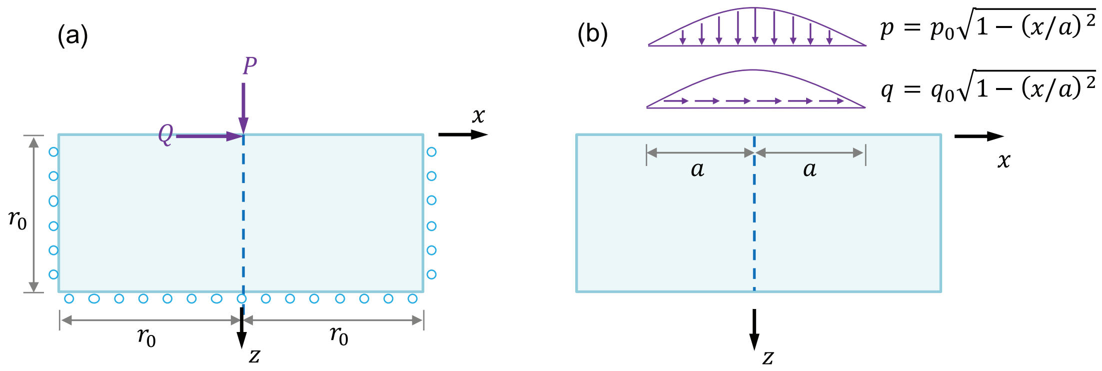

Fig. 2. Illustrative diagram of an elastic half-space subjected to (a) concentrated forces and (b) Hertzian distributed tractions.

no displacements, and the surface is subjected to external loadings at the center. Supposing that the external loadings are small, the boundary effects vanish and the theories of plane strain and elastic half-space apply. For a concentrated force P that acts in the direction normal to the surface, the vertical displacement u_z of the half-space is given as [12]

$$u_{z|x=0} = \frac{1-\nu^2}{E}\frac{2P}{\pi}\log(r_0/|z|) \tag{8}$$

$$u_{z|z=0} = \frac{1-\nu^2}{E}\frac{2P}{\pi}[\log(r_0/|x|) - 1/2(1-\nu)] \tag{9}$$

where ν and E are the Poisson's ratio and Young's modulus of the half-space, respectively; $|x|$ and $|z|$ represent the absolute values of coordinates x and z, respectively. It should be noted that for concentrated forces, there is no deformation at the origin (i.e., the limits of $u_{z|x=0}$ and $u_{x|z=0}$ at the origin do not exist). Similarly, the horizontal displacement u_x due to a tangential concentrated force Q is given as [12]

$$u_{x|x=0} = \frac{1-\nu^2}{E}\frac{2Q}{\pi}[\log(r_0/|z|) - 1/2(1-\nu)] \tag{10}$$

$$u_{x|z=0} = \frac{1-\nu^2}{E}\frac{2Q}{\pi}\log(r_0/|x|) \tag{11}$$

Considering a Hertzian distributed normal traction given by $p = (2N/\pi a)(1-x^2/a^2)^{1/2}$ (i.e., the form of Eq. (1) for the Hertzian normal contact stress), the vertical displacement at the origin due to this traction can be obtained by substituting it into Eq. (9) and integrating within the contact plane, such that

$$u_{z|x=0,z=0} = \int_{-a}^{a}\frac{1-\nu^2}{E}\frac{4N}{\pi^2 a}(1-x^2/a^2)^{1/2}[\log(r_0/|x|) - 1/2(1-\nu)]dx = \frac{1-\nu^2}{E}\frac{2N}{\pi}[\log(2r_0/a) - \nu/2(1-\nu)] \tag{12}$$

In addition, considering a Hertzian distributed tangential traction given by $q = (2T^{(a)}/\pi a)(1-x^2/a^2)^{1/2}$ (i.e., one of the terms in Eq. (2) for the Hertzian tangential contact stress), the horizontal displacement at the origin subjected to this traction is obtained as

$$u_{x|x=0,z=0} = \int_{-a}^{a}\frac{1-\nu^2}{E}\frac{4T^{(a)}}{\pi^2 a}\left(1-x^2/a^2\right)^{1/2}[\log(r_0/|x|)]dx = \frac{1-\nu^2}{E}\frac{2T^{(a)}}{\pi}[\log(2r_0/a) + 1/2] \tag{13}$$

The software *wolframalpha* has been used to obtain the analytical expression of the integrals.

2.3. Hertzian distributed loading on a half-round body

Next, the deformation of a half-round body subjected to Hertzian distributed tractions is studied. Fig. 3 shows the diagram of a half-round body. The top of the body is trimmed off by a small height to create a plane, where Hertzian distributed tractions are applied.

As illustrated in Fig. 4(a), the stress in the half-round body due to a Hertzian distributed normal traction can be considered as a combination of three contributions [12]: (1) the stress in a half-space due to the same Hertzian distributed normal traction; (2) the stress in a half-space due to the same amount of Hertzian distributed normal traction but is applied at the symmetric side; and (3) the stress in a complete round body due to a uniform surface normal traction $-N/\pi R$, where N is the total force integrated from the Hertzian distributed normal traction. Thus, the deformation of the half-round body could be approximated as a combination of the deformations due to these three contributions, such that

$$u_z^{(1)} = \frac{1-\nu^2}{E}\frac{2N}{\pi}[\log(2R/a) - \nu/2(1-\nu)] \tag{14}$$

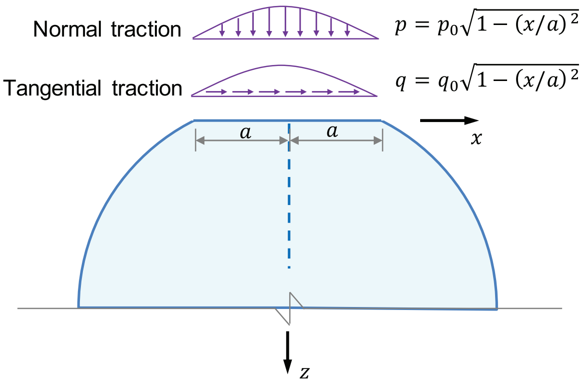

Fig. 3. Illustrative diagram of a half-round body subjected to Hertzian distributed tractions.

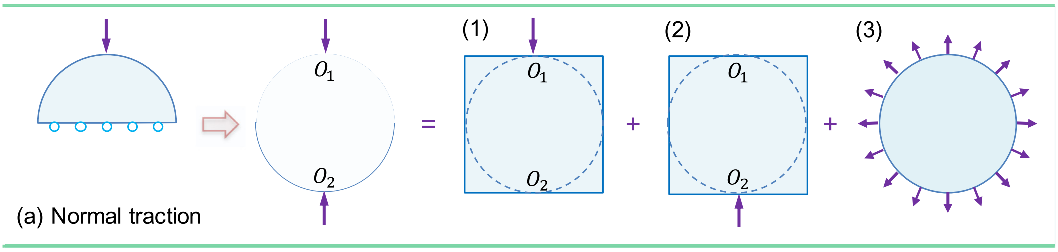

(a) Normal traction

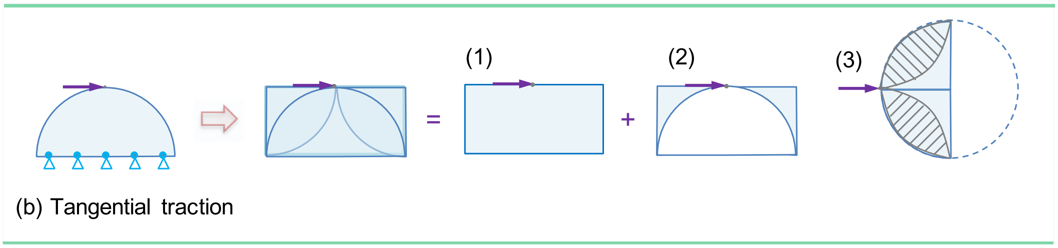

(b) Tangential traction

Fig. 4. Solution of the deformation of a half-round body due to (a) a Hertzian distributed normal traction and (b) a Hertzian distributed tangential traction.

$$u_z^{(2)} = \frac{1-\nu^2}{E}\frac{2N}{\pi}\log(2) \tag{15}$$

$$u_z^{(3)} = \frac{1-\nu^2}{E}\frac{2N}{\pi}[-1/2+\nu/2(1-\nu)] \tag{16}$$

$$u_z^{(p)} = u_z^{(1)} + u_z^{(2)} + u_z^{(3)} = \frac{1-\nu^2}{E}\frac{2N}{\pi}[\log(4R/a)-1/2] \tag{17}$$

where $u_z^{(p)}$ is the vertical displacement at the top of the body. Term $u_z^{(1)}$, corresponding to contribution (1), is the deformation of the half-space due to the Hertzian distributed normal traction and is obtained from Eq. (12). Term $u_z^{(2)}$, corresponding to contribution (2), is the deformation at point O_1 of the half-space due to the Hertzian distributed normal traction centered at point O_2, which can be considered as a concentrated force at point O_2 in view of the large distance between O_1 and O_2. $u_z^{(2)}$ can be calculated from Eq. (8) by substituting r_0 with R and z with $2R$. Term $u_z^{(3)}$, corresponding to contribution (3), is the deformation of the complete round body due to a uniform surface normal traction (see Appendix B). The obtained force-displacement relationship, given by Eq. (17), is exactly the same as the Johnson's solution [12]. Nevertheless, the derivation in this work is based on the combination of deformations whereas the Johnson's solution is based on the approach of stress and strain integration (see Appendix A).

The deformation of the half-round body subjected to a Hertzian distributed tangential traction is more challenging, and currently, no analytical functions are available. In this work, it is proposed to approximate the deformation as a combination of two contributions, namely (1) the deformation of a half-space and (2) the deformation of the difference of a half-space and a half-round body, respectively, due to the Hertzian distributed tangential traction, as illustrated in Fig. 4(b). The rationale behind this approximation is that without the resistance from contribution (2), the deformation of the half-space would be enlarged and approach the deformation of the half-round body. Since solving the deformation of contribution (2) is also a non-trivial problem, contribution (2) is then approximated as the deformation of a half-round body due to a Hertzian distributed normal traction multiplied by a penalty factor. The penalty factor accounts for the contribution of the shaded area in the half-round body shown in Fig. 4(b)-(3). To this end, the deformation of the half-round body due to the Hertzian distributed tangential traction is finally calculated as

$$u_x^{(1)} = \frac{1-\nu^2}{E}\frac{2T}{\pi}[\log(2R/a)+1/2] \tag{18}$$

$$u_x^{(2)} = wu_x^{(3)} = w\frac{1-\nu^2}{E}\frac{2T}{\pi}[\log(4R/a)+\nu/2(1-\nu)] \tag{19}$$

$$u_x^{(q)} = u_x^{(1)} + u_x^{(2)} = \frac{1-\nu^2}{E}\frac{2T}{\pi}[\log(2R/a)+1/2+w(\log(4R/a)+\nu/2(1-\nu)])] \tag{20}$$

where $u_x^{(q)}$ is the horizontal displacement at the top of the body; T is the total force of the tangential traction; terms $u_x^{(1)}$, $u_x^{(2)}$ and $u_x^{(3)}$ are the deformations corresponding to contributions (1), (2) and (3), respectively; and w is the penalty factor bounded between 0 and 1. Term $u_x^{(1)}$, which is the deformation of the half-space due to the Hertzian distributed tangential traction, can be obtained from Eq. (13). Term $u_x^{(3)}$ is the deformation of the half-round body due to the Hertzian distributed normal traction, and similar to the formulation of Eq. (17), $u_x^{(3)}$ is calculated as

$$u_x^{(3)} = \left\{\frac{1-\nu^2}{E}\frac{2T}{\pi}[\log(2R/a)+1/2]\right\} + \left\{\frac{1-\nu^2}{E}\frac{2T}{\pi}\log(2)\right\} + \left\{\frac{1-\nu^2}{E}\frac{2T}{\pi}[-1/2+\nu/2(1-\nu)]\right\} \tag{21}$$

where the three terms on the left side come from Eqs. (13), (8), and (B.2), respectively. By observing Eq. (19), it is found that $u_x^{(2)}$ is proportional to the Young's modulus and is nonlinearly correlated with the Poisson's ratio and term R/a. Such relations imply that the penalty factor, which accounts for the proportion between $u_x^{(2)}$ and $\frac{1-\nu^2}{E}\frac{2T}{\pi}[\log(4R/a)+\nu/2(1-\nu)]$, is likely a function of the Poisson's ratio and term R/a and is independent of the Young's modulus. The exact value of the penalty factor depends on the contribution of the shaded area and will be studied in the numerical results section.

3. Proposed Hertzian frictional contact model

3.1. Particle-particle contact

The Hertzian frictional contact model for a particle-particle contact is obtained by combining the normal and tangential force-displacement behaviors of two round bodies, with special consideration of the full slip or partial slip conditions of the contact. With recourse to the deformation of a half-round body subjected to a Hertzian normal traction (see Eq. (17)), the normal contact deformation δ_n due to a normal contact force N for a particle-particle contact is calculated as

$$\delta_n = \frac{1-\nu_1^2}{E_1}\frac{2N}{\pi}[\log(4R_1/a)-1/2] + \frac{1-\nu_2^2}{E_2}\frac{2N}{\pi}[\log(4R_2/a)-1/2] \tag{22}$$

Supposing that the two particles in contact have similar mechanical properties, it is then reasonable to replace the terms $(1-\nu_1^2)/E_1$ and $(1-\nu_2^2)/E_2$ with the composite modulus $E^\star$ defined in Eq. (5), which gives

$$\delta_n = \frac{N}{\pi E^\star}[\log(4R_1/a)+\log(4R_2/a)-1] \tag{23}$$

As to the tangential force-displacement behavior, the contact may be presented as a partial slip or full slip depending on the extent of the relative tangential displacement [12]. In the case of a partial slip state, by substituting $T^{(a)}$ in Eq. (13) with μN and $(c^2/a^2)\mu N$, respectively, the tangential contact deformation δ_t due to the tangential contact force is obtained as

$$\delta_t = \delta_t^{(a)} - \delta_t^{(c)} \tag{24}$$

$$\delta_t^{(a)} = \frac{\mu N}{\pi E^\star}\left[(\log(2R_1/a)+\log(2R_2/a)+1+w_1^{(a)}(\log(4R_1/a)+\nu_1/2(1-\nu_1))+w_2^{(a)}(\log(4R_2/a)+\nu_2/2(1-\nu_2))\right] \tag{25}$$

$$\delta_t^{(c)} = \frac{(c^2/a^2)\mu N}{\pi E^\star}\left[(\log(2R_1/c)+\log(2R_2/c)+1+w_1^{(c)}(\log(4R_1/c)+\nu_1/2(1-\nu_1))+w_2^{(c)}(\log(4R_2/c)+\nu_2/2(1-\nu_2))\right] \tag{26}$$

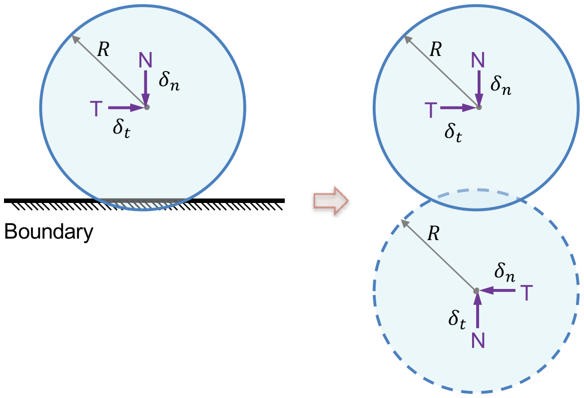

Fig. 5. Diagram of converting a particle-boundary contact to a particle-particle contact.

where $\delta_t^{(a)}$ and $\delta_t^{(c)}$ are the displacements corresponding to components μN and $(c^2/a^2)\mu N$, respectively, and $w_1^{(a)}$, $w_2^{(a)}$, $w_1^{(c)}$ and $w_2^{(c)}$ are the penalty factors, which can have different values depending on the specific contact geometric features and contact mechanical properties. In the case of a full slip state, the stick zone vanishes. The tangential force equals μN, and the tangential contact deformation is calculated as

$$\delta_t = \delta_t^{(a)} = \frac{\mu N}{\pi E^\star}\Big[(\log(2R_1/a) + \log(2R_2/a) + 1 + w_1^{(a)}(\log(4R_1/a) + \nu_1/2(1-\nu_1)) + w_2^{(a)}(\log(4R_2/a) + \nu_2/2(1-\nu_2))\Big] \tag{27}$$

It should be noted that in this case, $\delta_t^{(a)}$ only represents the deformation at the onset of a full slip state, or the maximum slip value. When a full slip state happens, the slide process develops with the contact zone moving along the particle boundary. It would lead to a new contact configuration, based on which the force-displacement behaviors should be reevaluated. The maximum slip value is given by the normal contact force, contact width and penalty factor, whereas it is eventually determined by the normal contact force. Unfortunately, an explicit and closed-form expression of the maximum slip value in terms of the normal contact force cannot be derived, as the contact width and the penalty factors are implicitly related to the normal contact force.

3.2. Particle-boundary contact

In DEM, boundaries (or the so-called walls) are used to applied force or displacement boundary conditions. They are often represented by line segments and are assumed to be rigid. Fig. 5 shows the scenario in which a particle is in contact with a boundary. Since boundaries are rigid and by virtue of symmetry, a particle-boundary contact can be converted into a particle-particle contact, with a slight modification on the relative displacements. In the particle-boundary contact case, the relative displacements are calculated as the displacements of particle centroid with respect to the boundary, so they are half of the relative displacements in the corresponding particle-particle contact case.

3.3. Consideration of loading history and model simplification

The derivations in Section 3.1 are based on a monotonically increasing tangential force while the normal force is kept constant. It should be noted that no matter how large or small the tangential force is, it would cause part of the contact to slip. Since slip is irreversible, it implies that the final stress and strain distributions in the contact will depend not solely upon the final values of the normal and tangential forces but also upon the loading history. For example, in the scenario in which the normal force is kept constant, and the tangential force is increased, the slipped zone would spread inwards from its inner edge, as shown in Fig. 6(a). If the tangential force is subsequently decreased, a secondary slip would start from the outer edge of the slipped zone and spread inwards instead of reversing the previous processing (i.e., starting from the inner edge of the slipped zone and spreading outwards). As a second example, if the tangential force is kept constant, to increase the normal force would not affect tangential stresses and deformations; on the other hand, to decrease the normal force would result in an enlargement of the slipped zone and a shrinkage of the stick zone in order to maintain an equilibrium of the tangential force (see Fig. 6(b)). By separating a complete loading history into a sequence of simple combinations (e.g., constant normal force and increasing tangential force, constant normal force and decreasing tangential force, increasing normal force and constant tangential force, etc.), it is possible to characterize the stress and strain distributions in the contact [12]. However, in DEM, contacts are dynamic with simultaneous variations of normal and tangential forces. It is difficult and also inefficient to consider the complete loading history of a contact. In order to facilitate the implementation and computational efficiency of DEM, this section presents a simplified version of the contact model developed in Section 3.1.

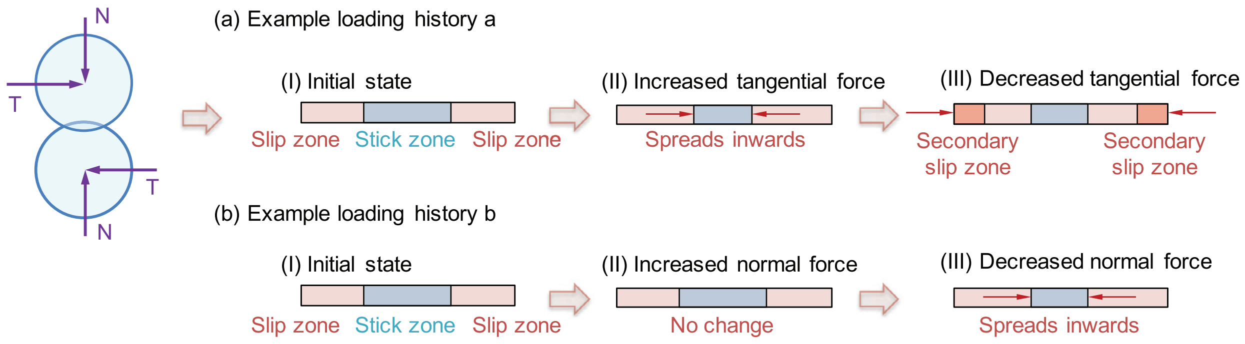

Fig. 6. Examples of the effects of loading history.

The normal force-displacement behavior of a contact is independent of the loading history. Thus, in the simplified model, the normal force-displacement equation given in Eq. (23) remains the same but is rewritten as (in the form that the displacement is given whereas the force is to be calculated)

$$N = k_n \delta_n \tag{28}$$

$$k_n = \pi E^\star [\log(4R_1/a) + \log(4R_2/a) - 1]^{-1} \tag{29}$$

where k_n is the normal contact stiffness, which is a variable that depends on the particle size and contact width. In the same manner, the tangential force-displacement behavior given in Eqs. (24) and (27) is rewritten as

$$T = k_t \delta_t \tag{30}$$

where k_t is the tangential contact stiffness and is a function of the particle size, contact width, stick zone width, and penalty factor. In fact, it is fairly difficult to derive an explicit form of k_t. However, it is noted that for a given pair of particles with a given constant normal contact force, the particle size, contact width, and penalty factor remain constants regardless of the tangential displacements. In this case, the tangential contact stiffness is then only varying with the stick zone width. As it will be illustrated in Section 4, the variation in the tangential contact stiffness with different stick zone widths is considerably small. Thus, in the simplified model, it is proposed to use the tangential contact stiffness at the onset of full slip to approximate the variable tangential contact stiffness throughout the full and partial slip states. In this regard, the tangential contact stiffness is calculated as

$$k_t = \pi E^\star \Big[(\log(2R_1/a) + \log(2R_2/a) + 1 + w_1^{(a)}(\log(4R_1/a) + \nu_1/2(1-\nu_1)) + w_2^{(a)}(\log(4R_2/a) + \nu_2/2(1-\nu_2)) \Big]^{-1} \tag{31}$$

It should be noted that although the tangential contact stiffness is assumed to be independent of the slip situations, the effects of the contact width is still incorporated in Eq. (31). Considering the effects of various normal contact forces, the tangential force-displacement behavior is given by an incremental displacement formulation

$$T = \min(T^0 + k_t \Delta\delta_t,\ \ \mu N) \tag{32}$$

where T^0 is the tangential contact force at the previous time step, $\Delta\delta_t$ is the incremental tangential displacement at the current time step, and k_t is the tangential contact stiffness corresponding to contact geometric features at the current time step. The Coulomb's law of friction is incorporated by comparing $T^0 + k_t \Delta\delta_t$ with μN.

To this end, the Hertzian frictional contact model has been developed with two versions, namely the accurate model in Section 3.1 and the simplified model in this section. The accurate model is applicable to the contact mechanics with monotonically increasing tangential force while the normal force is kept constant, whereas the simplified model neglects the partial slip effects and is suitable for DEM modeling.

3.4. Summary of the proposed model and implementation in DEM

In DEM, the contact deformations are known, whereas the contact forces are to be solved. The proposed model can be directly implemented into a DEM platform without the need to modify other modules of the code. For the ease of discussion, the equations of the proposed Hertzian friction contact model are summarized in Table 1. Since the contact forces are implicitly determined by these equations, the procedures for solving the contact forces are implemented as follows. First, given a normal displacement, the normal contact force and contact half-width are determined by solving Eqs. (4), (29) and (28). The Newton's iterative method can be employed to solve these implicit equations. Then, the penalty factors and tangential contact stiffness are calculated using Eqs. (33) and (31), respectively. Finally, given the tangential contact force

Table 1
Summary of the proposed Hertzian friction contact model for the implementation in DEM.

Category	Equations	Reference
Normal	$N = k_n \delta_n$	Eq. (28)
	$k_n = \pi E^\star [\log(4R_1/a) + \log(4R_2/a) - 1]^{-1}$	Eq. (29)
Tangential	$T = \min(T^0 + k_t \Delta\delta_t,\ \mu N)$	Eq. (32)
	$k_t = \pi E^\star \left[(\log(2R_1/a) + \log(2R_2/a) + 1 + w_1^{(a)}(\log(4R_1/a) + \nu_1/2(1-\nu_1)) + w_2^{(a)}(\log(4R_2/a) + \nu_2/2(1-\nu_2))\right]^{-1}$	Eq. (31)
Contact half-width	$a = [(4NR^\star)/(\pi E^\star)]^{1/2}$	Eq. (4)
Penalty factor	$w_{1,2}^{(a)} = 0.22 + 2.89(a/R_{1,2}) + 0.18\nu_{1,2} - 10.31(a/R_{1,2})^2 + 1.75(a/R_{1,2})\nu_{1,2} + 0.36\nu_{1,2}^2$	Eq. (33)
Composite E and R	$E^\star = \left[(1-\nu_1^2)/E_1 + (1-\nu_2^2)/E_2\right]^{-1}$	Eq. (5)
	$R^\star = [1/R_1 + 1/R_2]^{-1}$	Eq. (6)

at the previous time step and the incremental tangential displacement at the current time step, the tangential contact force at the current time step is updated using Eq. (32). Compared with the conventional linear spring contact model, the new model is computationally more expensive. However, as it has been described in the previous sections, the Hertzian contact model has the advantages that it can accurately capture the nonlinear force-displacement behaviors of particle contacts and that the contact stiffness has a direct correlation with the common mechanical properties such as Young's modulus and Poisson's ratio.

It should be noted that the contact model only describes the force-displacement relationships within the partially slip and the onset of fully slip regimes. As aforementioned, as the slide process develops, the contact zone moves along the particle boundary and thus the force-displacement behaviors should be reevaluated based on the new contact configuration. In DEM, the effects of finite slide on the force-displacement behaviors are not explicitly considered but are incorporated via time integration. In every time step of a DEM simulation, the contact configuration is first updated and the force-displacement behaviors are calculated based on the updated contact configuration. The force-displacement behaviors based on time integration would be fairly accurate if the timestep is reasonably small, which is often the case of a DEM simulation. In addition, it is noted that the derivation in this work is based on the Hertz and elasticity theories with small deformations. The accuracy of the proposed model would be negatively impacted when it is applied to deformable particles with large contact deformations. Moreover, in the current implementation of DEM, the particle deformation due to contact is assumed to be localized and do not affect other particle contacts. This assumption is justified if the deformation of real particles is relatively small [40]. Recently, there have been attempts (the so-called multiple-contact modeling approaches) to extend the contact modeling by taking into account the effect of neighboring particles [41–43]. The basic idea is to incorporate the mutual influence of multiple contacts. For example, Rojek et al. [43] developed a deformable DEM, in which the deformed shape of a particle is first obtained by strain integration and then the contact behavior between particles is evaluated based on the deformed shape. Another option is to first calculate the displacement fields induced by every other contact of a particle using elasticity theories, and then add the particle deformation of other contacts to a local contact [41,42]. The contact behavior at the local contact is evaluated using the add-up contact deformations. The contact model proposed in this work establishes a semianalytical relationship between the contact forces and contact deformations. It can be readily employed by the multiple-contact modeling approaches following the same way as the contact models that have used in these aforementioned works.

4. Numerical examples and discussion

In this section, three numerical examples are presented to characterize the penalty factor and validate the proposed contact model. The first two examples focus on sub-particle analyses, in which the results evaluated from the proposed contact model are compared with those obtained from the finite element analyses. The third example considers a full DEM simulation of the bi-axial compression test on polydispersed particles.

4.1. Half-round body subjected to tangential traction

The first example studies the deformation of a half-round body subjected to a Hertzian distributed tangential traction, as previously shown in Fig. 3. The body has a radius of 0.5 m, and the contact plane has a half-width of 0.025 m, which is approximately 5% of the body radius. The Young's modulus of the body is set to 10 GPa, and the Poisson's ratio is 0.25. A Hertzian distributed tangential traction is applied on the contact plane and has a total force of 10^5 N/m. Parametric studies are performed on the body radius, contact width, Young's modulus, and Poisson's ratio to investigate the effects of these parameters on the penalty factor. In each of the parametric studies, one parameter is varied within a practical range while the other parameters are kept constant. The commercial software COMSOL is adopted to run the finite element method (FEM)-based simulations. With the body deformation evaluated from the FEM simulations as a benchmark, the penalty factors are solved from the semianalytical force-displacement relationship (i.e., Eq. (20)) developed in this work. The penalty factors in the cases of different contact geometric features and mechanical properties are gathered in Fig. 7.

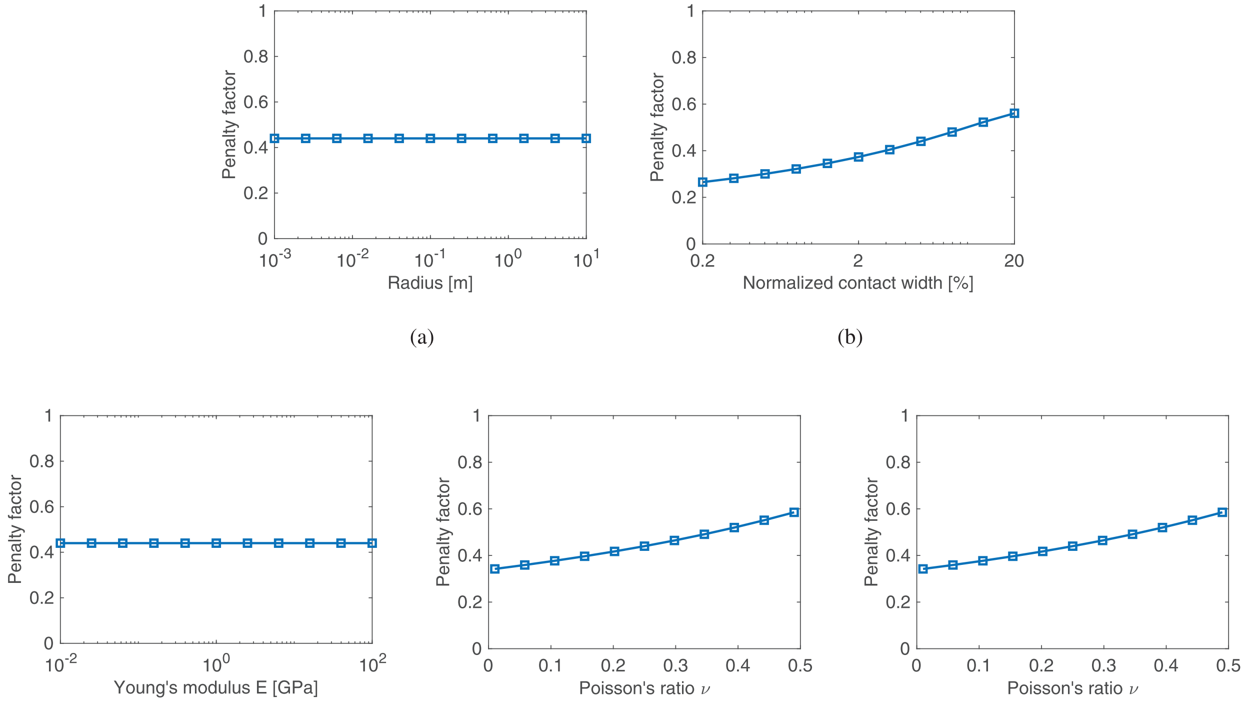

(a) (b)

(c) (d) (e)

Fig. 7. The penalty factor in the cases of different contact geometric features and mechanical properties: (a) body radius, (b) contact width, (c) Young's modulus, (d) Poisson's ratio, and (e) different Poisson's ratio and Young's modulus while $E/(1-\nu^2)$ is kept constant. The normalized contact width is defined as the contact half-width divided by the body radius.

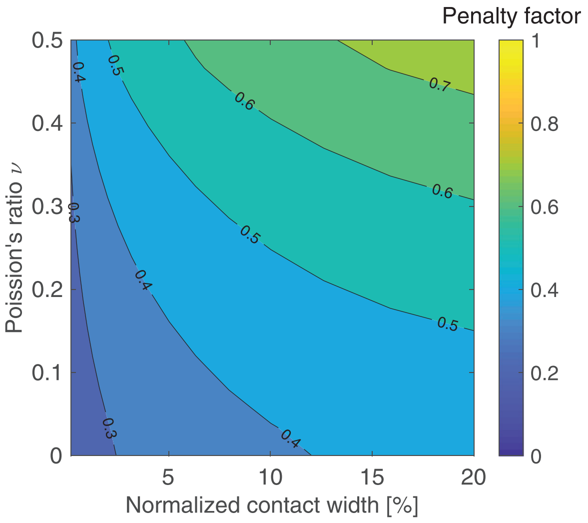

Fig. 8. The penalty factor in the cases of different combinations of contact widths and Poisson's ratios.

The results indicate that the penalty factor is independent of the body size and Young's modulus, whereas it increases with contact width and Poisson's ratio.

Considering that the penalty factor is only affected by the contact width and Poisson's ratio (shown in Fig. 7), the joint effects of these two parameters on the penalty factor are investigated. The penalty factors for a grid set of contact widths and Poisson's ratios are calculated and plotted in Fig. 8. Overall, the penalty factor stays within a range of about 0.25–0.75, and the average is approximately 0.5. Based on the results presented in Fig. 8, an empirical equation of the penalty factor is

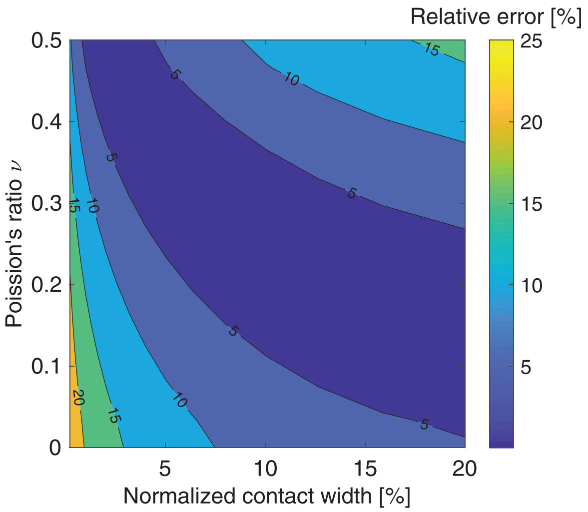

Fig. 9. The relative errors in the calculated tangential displacement at a given tangential force if a constant penalty factor of 0.5 is used.

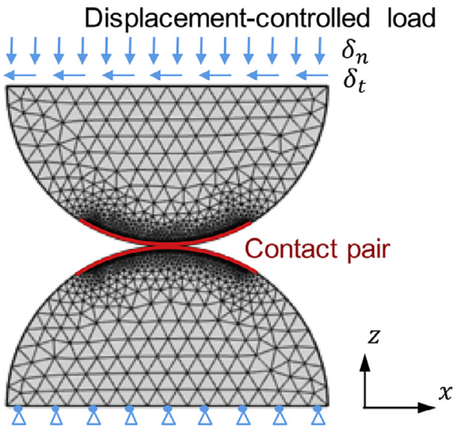

Fig. 10. Model setup of the single particle-particle contact problem.

obtained as

$$w = 0.22 + 2.89(a/R) + 0.18\nu - 10.31(a/R)^2 + 1.75(a/R)\nu + 0.36\nu^2 \tag{33}$$

where a is the contact half-width, ν is the Poisson's ratio, and R is the body radius. The coefficient of determination (i.e., R-square) of the fitting is about 0.97. It should be noted that other types of equations can be adopted for the fitting as well. Nonetheless, the adopted binary quadratic equation is simple and could provide a fairy good approximation. It is also applicable to different material properties and test cases as the parametric studies have covered a wide range of material properties and contact geometric features.

Since the empirical equation might not be convenient for practical usage, this section further investigates the errors in the calculated tangential forces and displacements if a constant penalty factor is used. Supposing that the penalty factor is taken the average value 0.5 in practice, the relative error in the displacement for a given force, calculated from Eq. (20), is found to be less than 25% (as shown in Fig. 9). On the other hand, if the displacement is given, the error in the calculated force is less than 20%. The results imply that if the tangential force-displacement behavior is to be evaluated with high accuracy, the penalty factor could be calculated from Eq. (33); otherwise, it might be acceptable to take the penalty factor as 0.5 for simplicity.

4.2. Single particle-particle contact test

The second example considers two particles in contact, as sketched in Fig. 10. Again, the software COMSOL is used to set up the FEM model. The particles have a radius of 0.5 m and are modeled in half by virtue of symmetry. The lower particle is fixed at the bottom, and the upper particle is specified with prescribed displacements at the top. The particle surfaces that would potentially come in contact are modeled as contact pairs [44]. A static Coulomb friction model is added to the

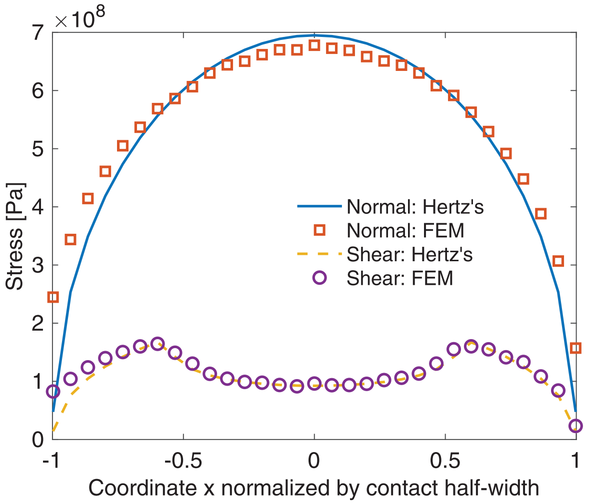

Fig. 11. The distribution of the normal and shear stresses in the contact plane at a partial slip state.

contact pair to model the slip and slide behaviors in the contact. The domain is discretized using a triangle mesh with the element size being smaller than 0.05 m and the edges of the contact pair are discretized using a denser mesh with the element size being at about 0.01 m. The resultant mesh contains 1701 nodes and 3104 triangle elements. To improve the convergence performance and the model accuracy, the linear shape function is selected for the displacement field to obtain an initial guess of the solution, based on which the FEM model is solved again using quadratic serendipity shape function to obtain a more accurate solution. For the material properties, the Young's modulus is 10 GPa, the Poisson's ratio is 0.25, and the contact friction is 0.3.

Two cases of loading histories are considered. In the first case, the prescribed vertical displacement, δ_n, is kept constant 0.025 m, which is 5% of the particle radius and will give rise to a contact half-width of about 13% of the particle radius. The prescribed horizontal displacement, δ_t, increases from 0 to 0.025 m using a parametric sweep. In the second case, the vertical and horizontal displacements are simultaneously increased to 0.025 m and 0.025 m, respectively, to simulate a case of simultaneously increased normal and tangential loads. It is worth noting that the first case of loading scenario is also a prospective scenario for conducting laboratory experiments, which could be used to validate the proposed contact model from the experimental perspective, or to measure the contact properties of cylindrical specimens. In this work, the force-displacement behaviors will be compared with FEM simulations to validate the proposed model. The experimental validation will be explored in future work.

4.2.1. The accurate model

For the first case of loading history, the accurate model developed in Section 3.2 applies. In order to verify the FEM model, the contact stresses extracted from the FEM simulation are compared with the analytical solution (i.e., Eqs. (1) and (2)) from the Hertz's theory. As discussed in Section 2, the normal stress in the contact plane follows an elliptical equation, and the shear stress is a combination of two elliptical equations. Fig. 11 shows the stress distributions in the contact plane when the tangential displacement is 0.01 m, i.e., 2% of the particle radius. At this tangential displacement, the contact partially slips. The stresses based on the FEM simulation are fairly consistent with those calculated from the Hertz's analytical solution.

Fig. 12 shows the evolution of the horizontal force due to the contact with increasing horizontal displacement. It should be pointed out that in this example, the horizontal force-displacement behavior is not necessarily the same with the tangential contact force-displacement behavior. Before the occurrence of the slide process, the contact plane is assumed to remain horizontal and the horizontal force is equal to the tangential contact force. When the slide process develops, the contact plane evolves and the horizontal force is a combination of the normal and tangential contact forces. The force-displacement behaviors of sphere contacts under this loading scenario has been theoretically studied in Balevičius and Mróz [45], 46]. Following the same approach, the force-displacement behaviors of cylinder contacts are derived in Appendix C. For both the results of the proposed contact model and FEM simulation, the horizontal force first increases (corresponding to the partial slip stage) and then slightly decreases (corresponding to the full slip and finite slide stages) with the increase of horizontal displacement. Such a decrease in the horizontal force is due to the evolution of the contact plane as the slide process develops. The tangential contact stiffness (i.e., the slope of the force-displacement curve) during the partially slip stage exhibits a slightly decreasing trend with increasing tangential displacement. Overall, the horizontal forces evaluated from the proposed contact model are a fairly good match with the results of the FEM simulation, with only slight discrepancies at large tangential displacements. Such discrepancies may result from the influence of the normal contact force as the contact plane

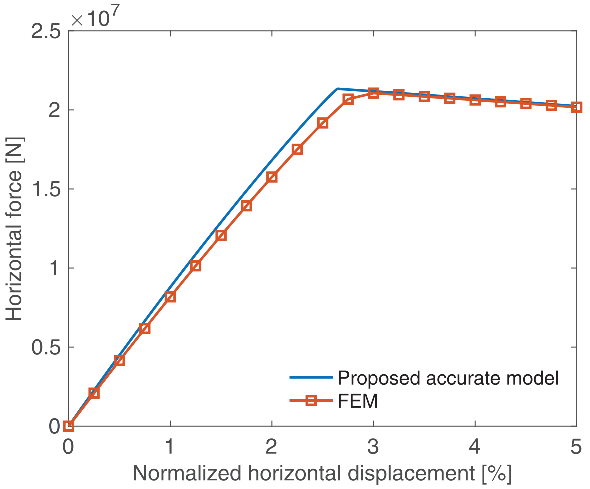

Fig. 12. The evolution of the horizontal force with increasing horizontal displacement. The horizontal displacement is normalized by the particle radius.

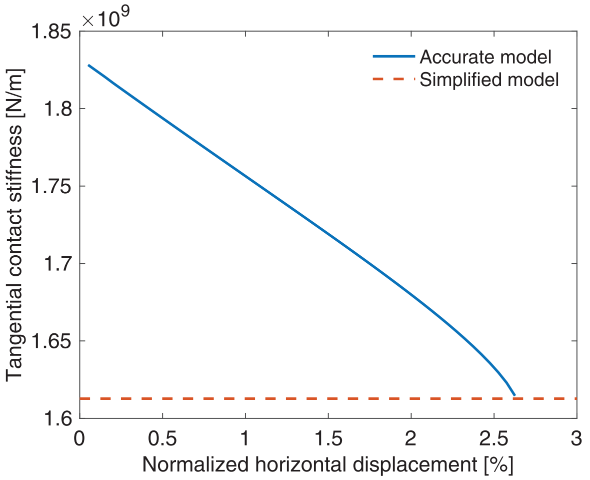

Fig. 13. The evolution of the tangential contact stiffness with the normalized horizontal/tangential displacement where the normal displacement is kept constant. The approximation of the tangential contact stiffness in the simplified model is plotted as a comparison.

becomes asymmetric with respect to the *z*-axis when a tangential displacement is applied. Nevertheless, the discrepancies between the proposed model and FEM simulation are considerably small.

4.2.2. The simplified model

Since the effects of loading history lie in the fact that slips are irreversible, it is then interesting to investigate that to what extent the force-displacement behavior would be affected by the slip of the contact. With the force-displacement curve shown in Fig. 12, the (secant) tangential contact stiffness is calculated, and the results are plotted in Fig. 13. Herein, the prefix secant indicates the secant slope of the force-displacement curve shown in Fig. 12. The (secant) tangential contact stiffness is shown to be decreasing with the increasing tangential displacement. Throughout the loading process, the (secant) tangential contact stiffness decreases by about 12%. In the simplified contact model, the tangential contact stiffness at a certain normal contact force is approximated by a constant value, i.e., the (secant) tangential contact stiffness at the onset of a full slip. Using the constant tangential contact stiffness, the evolution of tangential force with increasing tangential stiffness is plotted in Fig. 14. The results of the simplified contact model match fairly well with the results of the FEM simulation.

As it has been discussed in Section 3.3 that although the tangential contact stiffness is assumed to be independent of the slip states in the simplified model, the effects of the contact width on the tangential contact stiffness is still incorporated. In the first case of loading history, the tangential contact stiffness is approximated by a constant for the given constant normal contact width. In the second loading history with various contact widths, the tangential stiffness would also vary accordingly. Fig. 15 shows the evolution of the normal and tangential contact forces in the case of simultaneously increasing normal and tangential contact displacements. It can be seen that both the normal and tangential force-displacement behav-

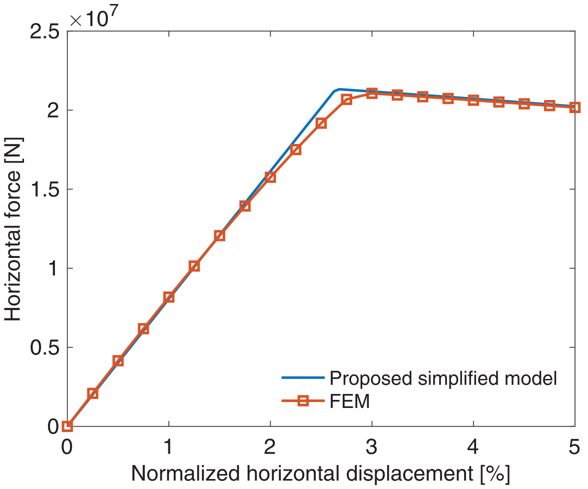

Fig. 14. The evolution of the horizontal force with increasing horizontal displacement based on the proposed simplified model.

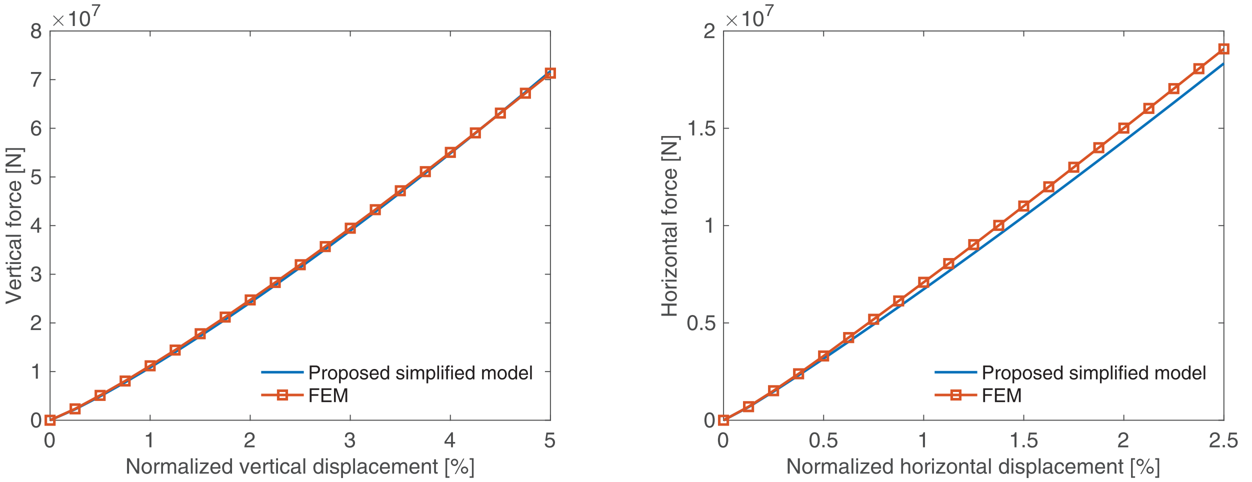

(a) (b)

Fig. 15. The evolution of the (a) vertical force and (b) horizontal force with simultaneously increasing vertical and horizontal displacements.

iors are nonlinear, with both the normal and tangential contact stiffness increasing with increasing normal displacement. Throughout the loading process, the slide regime is not attained. The results of the simplified contact model match fairly well with the results of the FEM simulations.

4.3. DEM simulation of bi-axial compression test

The last example considers the DEM simulation of the bi-axial compression test on polydispersed particles. The proposed contact model is implemented in an in-house DEM code, and the purpose of this numerical example is to demonstrate the performance of the proposed contact model in the DEM simulations of particulate systems. As shown in Fig. 16, a total of 200 round particles of sizes ranging from 0.06 m to 0.08 m are firstly randomly placed in a box of width 1.0 m and height 1.5 m. The particles are then allowed to settle down at gravity for 5.0 s to form a stable packing. After that, a boundary wall is placed on the top of the packing and the packing are compressed with two stages, i.e., an isotropic compression stage and a shearing stage. In the isotropic compression stage, the lateral and top walls are moved inwards to achieve an isotropic compression pressure of 0.1 GPa via a servo control mechanism. The isotropic stage lasts for 1.0 s. In the shearing stage, the top wall is moved down at a velocity of 0.1 m/s whereas the lateral walls are adjusted via the servo control mechanism to maintain the lateral confining pressure at 0.1 GPa. The shearing stage lasts for 2.0 s, which accounts for an axial strain of about 20%. Throughout the packing and compression processes, the following parameters are used: the particle density is 2700 Kg/m^3, Young's modulus is 10 GPa, Poisson's ratio is 0.25, contact friction is 0.3, contact damping is 0.7, and the

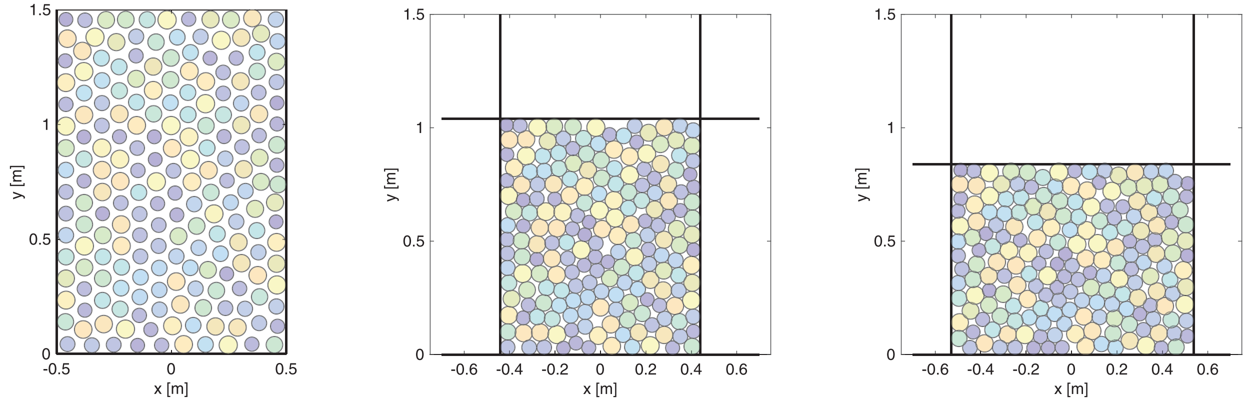

(a) (b) (c)

Fig. 16. Snapshots of the DEM simulation at (a) the beginning of packing process, (b) the end of isotropic compression stage, and (c) the end of shear stage. The color of the particles represents the particle diameters.

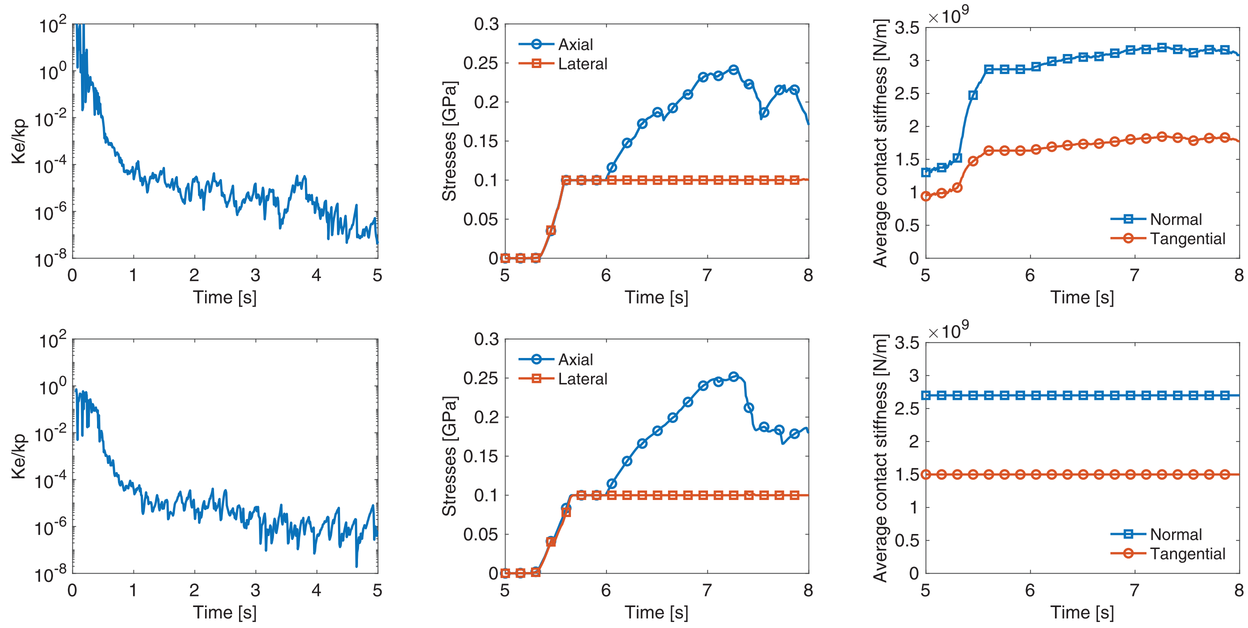

(a) (b) (c)

Fig. 17. Quantitative analyses of the DEM simulation: (a) the ratio of kinetic energy to contact potential energy during the packing process, (b) the evolution of axial stress and lateral stress during the compression process, and (c) the evolution of the (average) normal contact stiffness (i.e., Eq. (29)) and tangential contact stiffness (i.e., Eq. (31)) during the compression process. The top row represents the results of the proposed Hertzian friction contact model and the bottom row represents the results of the linear spring contact model.

timestep is fixed at 1×10^{-5} s. As a comparison, the bi-axial compression test with the linear spring contact model is also conducted. The normal and tangential contact stiffness for the linear spring contact model are set to 2.7×10^{9} N/m and 1.5×10^{9} N/m, respectively, which are determined from a linear regression of the force-displacement results presented in Fig. 15. The other parameters are kept the same.

Three quantitative analyses of the DEM simulation are reported in Fig. 17. The first is the ratio of kinetic energy to contact potential energy during the packing process, as shown in Fig. 17a. The relative kinetic energy diminishes rapidly as the particles assembly approaches its quasi-static equilibrium state. The results of proposed Hertzian contact model and linear spring model exhibit fairly similar profiles. The second is the evolution of the axial and lateral stresses during the compression process, as shown in Fig. 17b. During the isotropic compression stage, the lateral and axial stresses increase from zero to 0.1 GPa and then maintain stably at 0.1 GPa. After that, the axial stress first increases nonlinearly with time, and then exhibits a sudden decrease after reaching a peak value. The residual strength of the linear spring contact model

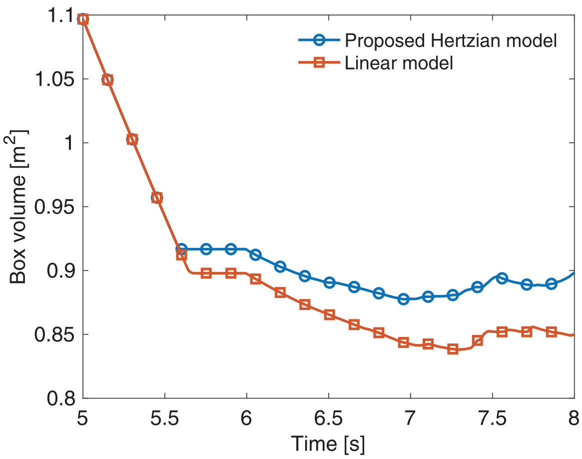

Fig. 18. The evolution of the volume of the box container during the compression process.

is slightly smaller than that of the Hertzian model. Nevertheless, the results of the Hertzian model and linear spring model exhibit fairly similar profiles. In Zhao et al. [24], it has been illustrated that with a proper calibration of the contact stiffness, the linear spring model is able to resemble the Hertzian model on aspects of both microscopic and macroscopic mechanical behaviours of granular media. However, the contact model and contact stiffness have a significant effect on the deformation behavior of granular media, which can be observed from Fig. 18. Compared with the linear spring model, the packing of the proposed Hertzian model exhibits a fairly larger volume (i.e., smaller volumetric strain) after compression. Lastly, the normal contact stiffness and tangential contact stiffness (averaged from all the particle-particle and particle-boundary contacts) at each time step is plotted in Fig. 17c. For the Hertzian model, the normal contact stiffness and tangential contact stiffness, respectively, are defined and calculated by Eqs. (29) and (31). As expected for the case of proposed Hertzian model, the contact stiffness increases with increasing particle penetration depth due to compression, which is the most notable feature that can be captured by the proposed Hertzian model. Overall, the quantitative analyses demonstrate the good stability and effectiveness of the proposed Hertzian model in a DEM simulation. The Hertzian model mainly affects the contact stiffness and thus the deformation behavior of granular media.

5. Conclusions

In this work, a semianalytical Hertzian frictional contact model is proposed for the computational contact mechanics in 2D. The proposed model consists of an analytical solution for the normal contact behavior and a semianalytical solution with a variable penalty factor for the tangential contact behavior. The Hertzian distributed contact stresses and the slip situations in the contact plane are explicitly considered. To facilitate the implementation and computational efficiency in DEM, a simplified formulation of the proposed contact model has also been provided. The simplified model considers only the effects of contact width on the tangential stiffness, whereas the effects of partial slip are neglected. Based on the results of finite element simulations, it is found that the penalty factor stays in the range of about [0.25, 0.75] for a variety of contact material properties. It is independent of the particle size and Young's modulus, whereas it increases with the contact width and Poisson's ratio. An empirical equation of the penalty factor with respect to the contact width and Poisson's ratio has then been provided. It has been shown that with the penalty factor calculated from the empirical equation, the proposed contact model can accurately capture the nonlinear contact behaviors of particles in 2D. It is also found that if a constant penalty factor of 0.5 is used, the error in the evaluated tangential contact forces is less than 20%. Lastly, the proposed contact model has been implemented in an in-house DEM code. Quantitative analyses of the DEM bi-axial compression test on polydispersed particles have demonstrated the good stability and effectiveness of the proposed Hertzian contact model. The proposed 2D Hertzian frictional contact model could be useful to the computational mechanics of particles in 2D. It is also applicable to parallel-axis cylinders with strip contacts, as a special case in 3D.

Acknowledgments

This work was supported by the Hong Kong Scholars Program (2020), the Fundamental Research Funds for the Central Universities (grant no. 19lgpy289), the National Natural Science Foundation of China (grant nos. 51678578, 51909289, 51978677), the China Postdoctoral Science Foundation (grant no. 2019M663240), and the Shenzhen Natural Science Foundation (grant no. JCYJ20190807162401662). These sources of financial support are gratefully acknowledged. The authors would also like to thank the Editor and reviewers for their constructive comments and suggestions to improve the manuscript.

Appendix A. Deformation of a half-round body subjected to a Hertzian distributed normal traction: the Johnson's solution

Considering a half-round body that is subjected to a Hertzian distributed normal traction $p = p_0(1 - x^2/a^2)^{1/2}$ at the top, the stresses in this body can be obtained by adding the stresses subjected to the three contributions described in Section 2.3, as

$$\sigma_x = -\frac{N}{\pi}\left(\frac{1}{R} - \frac{2(a^2 + 2z^2)}{a^2(a^2 + z^2)^{1/2}} + \frac{4z}{a^2}\right) \tag{A.1}$$

$$\sigma_z = -\frac{N}{\pi}\left(\frac{1}{R} - \frac{2}{2R - z} - \frac{2}{(a^2 + z^2)^{1/2}}\right) \tag{A.2}$$

where σ_x and σ_z are the stresses in the horizontal and vertical directions, respectively, and N is the total force corresponding to traction p. With the plane strain condition, the vertical stain ϵ_z of the body can be calculated as

$$\epsilon_z = \frac{1 - \nu^2}{E}\left(\sigma_z - \frac{\nu}{1 - \nu}\sigma_x\right) \tag{A.3}$$

The vertical displacement of the body top is then found by integrating ϵ_z from the centroid to the surface, such that

$$\delta_n = \int_0^R \frac{1 - \nu^2}{E}\left(\sigma_z - \frac{\nu}{1 - \nu}\sigma_x\right)dz = \frac{1 - \nu^2}{E}\frac{2N}{\pi}[\log(4R/a) - 1/2] \tag{A.4}$$

Appendix B. Deformation of a round body with the surface subjected to a uniform normal traction

Considering a round body with the surface subjected to a uniform normal traction $N/\pi R$, the stresses in the body are then given as

$$\sigma_x = \sigma_z = \frac{N}{\pi R} \tag{B.1}$$

Thus, the normal deformation δ_n of the body surface with respect to the centroid can be calculated as

$$\delta_n = \int_0^R \frac{1 - \nu^2}{E}\left(\frac{N}{\pi R} - \frac{\nu}{1 - \nu}\frac{N}{\pi R}\right)dz = \frac{1 - \nu^2}{E}\frac{2N}{\pi}[1/2 - \nu/2(1 - \nu)] \tag{B.2}$$

Appendix C. Cylinder transverse translation along a linear trajectory

As shown in Fig. C.19, the scenario contains two cylinders with the lower cylinder being fixed and the upper cylinder moving along a liner trajectory. The rotational motions of both cylinders are restricted. Initially, the cylinders are compressed, inducing a predefined value of normal contact deformation h_0^δ. With the increase of the transverse translation of the upper cylinder, the contact behavior transits from slip regime into slide regime. Before the slide process occurs, the contact plane only exhibits micro slips and the orientation of the contact plane is assumed to remain the same. At this stage, the horizontal force-displacement behavior can be directly characterized by the proposed contact force-displacement equations summarized in Table 1. When the slide process occurs and develops, the contact plane moves along the cylinder boundary and the orientation of the contact plane evolves accordingly. Following a similar approach presented in Balevičius and Mróz [45], 46], the force-displacement behaviors for cylinder transverse translation along a linear trajectory are derived as follows.

Based on an instant contact configuration, the equilibrium equations of the upper cylinder can be written as:

$$\Sigma F_x = 0,\ F - \mu N\cos\alpha + N\sin\alpha = 0 \tag{C.1}$$

$$\Sigma F_y = 0,\ -N^* + \mu N\sin\alpha + N\cos\alpha = 0 \tag{C.2}$$

where F and N^* represent the horizontal and vertical driving forces, respectively; N is the contact normal force, α is the rotation angle of the contact normal orientation with respect to the original contact normal orientation. Solving for the horizontal driving force gives

$$F = \mu N\cos\alpha - N\sin\alpha \tag{C.3}$$

The contact deformations can be related to the driving horizontal displacement through the following decomposition scheme (see Fig. C.19)

$$\delta_{su} = (S_t - y_0\tan\alpha)\cos\alpha \tag{C.4}$$

$$\delta_n = R_1 + R_2 - (y_0/\cos\alpha + \delta_{su}\tan\alpha) \tag{C.5}$$

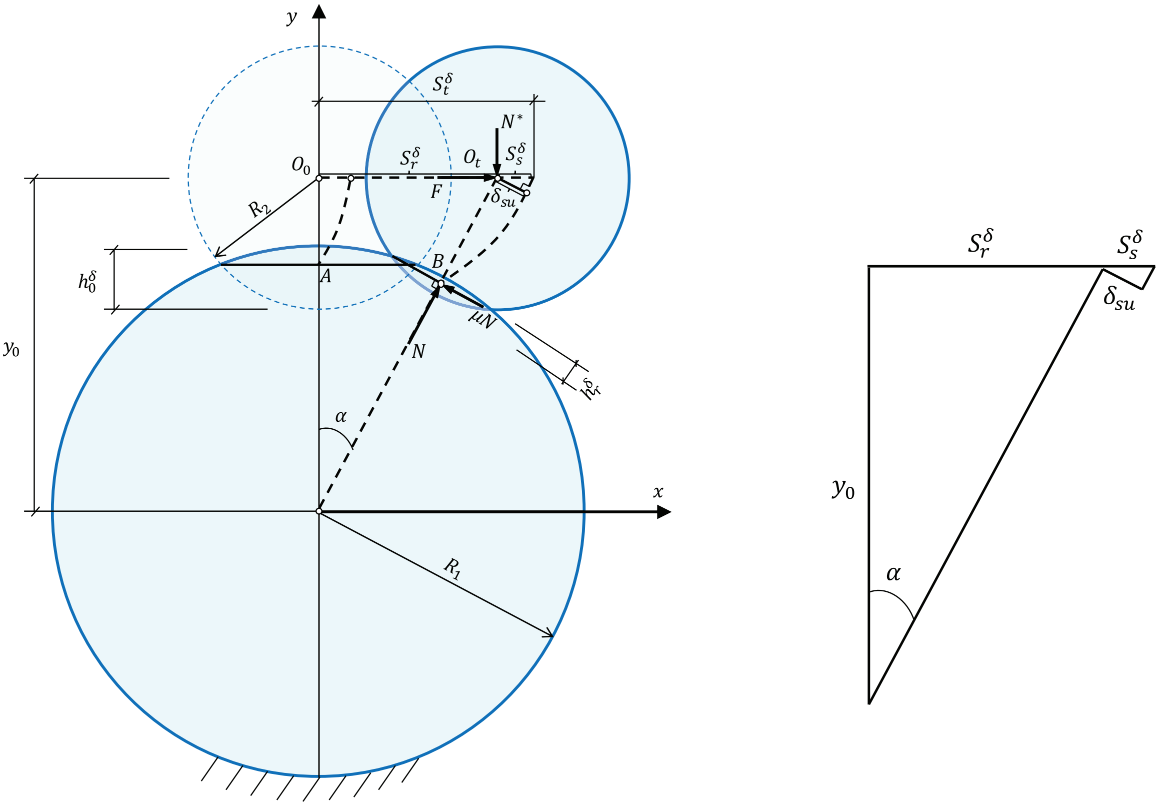

Fig. C.19. Cylinder transverse motion along a linear trajectory under the displacement-controlled process. Adapted from [46].

where δ_{su} is the ultimate slip deformation (i.e., the tangential displacement at the onset of full slip), δ_n is the contact normal deformation, S_t is the driving horizontal displacement, and y_0 is the initial distance of the cylinder centroids. Given the driving horizontal displacement S_t, the unknowns δ_{su}, δ_n, α, N can be solved by combining (C.4) and (C.5), the contact force-displacement equations in Table 1, and the Coulomb friction rule. Then, the horizontal force can be calculated from (C.3).

References

[1] P.A. Cundall, O.D.L. Strack, A discrete numerical model for granular assemblies, Géotechnique 29 (1) (1979) 47–65.
[2] P.W. Cleary, M.L. Sawley, DEM modelling of industrial granular flows: 3D case studies and the effect of particle shape on hopper discharge, Appl. Math. Model. 26 (2) (2002) 89–111.
[3] H.P. Zhu, Z.Y. Zhou, R.Y. Yang, A.B. Yu, Discrete particle simulation of particulate systems: a review of major applications and findings, Chem. Eng. Sci. 63 (23) (2008) 5728–5770.
[4] Z. Lai, Q. Chen, Characterization and discrete element simulation of grading and shape-dependent behavior of JSC-1A martian regolith simulant, Granul. Matter 19 (4) (2017) 69.
[5] K. Taghizadeh, S. Luding, V. Magnanimo, DEM applied to soil mechanics, in: ALERT Doctoral School 2017 Discrete Element Modeling, 2017, p. 129.
[6] Y. Xia, Z. Lai, T. Westover, J. Klinger, H. Huang, Q. Chen, Discrete element modeling of deformable pinewood chips in cyclic loading test, Powder Technol. 345 (2019) 1–14.
[7] Y. Xia, J.J. Stickel, W. Jin, J. Klinger, A review of computational models for the flow of milled biomass I: discrete-particle models, ACS Sustain. Chem. Eng. (2020).
[8] J. Yang, Y.M. Low, C.-H. Lee, Y.-M. Chiew, Numerical simulation of scour around a submarine pipeline using computational fluid dynamics and discrete element method, Appl. Math. Model. 55 (2018) 400–416.
[9] A.B. Yu, Discrete element method, Eng. Comput. (2004).
[10] Y. Guo, J.S. Curtis, Discrete element method simulations for complex granular flows, Annu. Rev. Fluid Mech. 47 (2015) 21–46.
[11] H. Hertz, Ueber die beruhrung fester elastischer korper (on the contact of elastic solids), J. Reine Angew.Math. 92 (1882) 156–171.
[12] K.L. Johnson, Contact Mechanics, Cambridge university press, 1987.
[13] A. Di Renzo, F.P. Di Maio, An improved integral non-linear model for the contact of particles in distinct element simulations, Chem. Eng. Sci. 60 (5) (2005) 1303–1312.
[14] B.K. Mishra, A review of computer simulation of tumbling mills by the discrete element method: part I – contact mechanics, Int. J. Miner. Process. 71 (1–4) (2003) 73–93.
[15] S. Luding, Cohesive, frictional powders: contact models for tension, Granul. Matter 10 (4) (2008) 235.
[16] M. Ucgul, J.M. Fielke, C. Saunders, Three-dimensional discrete element modelling of tillage: determination of a suitable contact model and parameters for a cohesionless soil, Biosyst. Eng. 121 (2014) 105–117.
[17] C. Thornton, S.J. Cummins, P.W. Cleary, An investigation of the comparative behaviour of alternative contact force models during elastic collisions, Powder Technol. 210 (3) (2011) 189–197.

[18] H.A. Navarro, M.P. de Souza Braun, Determination of the normal spring stiffness coefficient in the linear spring–dashpot contact model of discrete element method, Powder Technol. 246 (2013) 707–722.
[19] X. Li, H. Yu, Fabric, force and strength anisotropies in granular materials: a micromechanical insight, Acta Mech. 225 (8) (2014) 2345–2362.
[20] Z. Lai, Q. Chen, L. Huang, Fourier series-based discrete element method for computational mechanics of irregular-shaped particles, Comput. Methods Appl. Mech.Eng. 362 (2020) 112873.
[21] J.-P. Plassiard, N. Belheine, F.-V. Donzé, A spherical discrete element model: calibration procedure and incremental response, Granul. Matter 11 (5) (2009) 293–306.
[22] C.J. Coetzee, Calibration of the discrete element method, Powder Technol. 310 (2017) 104–142.
[23] A. Di Renzo, F.P. Di Maio, Comparison of contact-force models for the simulation of collisions in DEM-based granular flow codes, Chem. Eng. Sci. 59 (3) (2004) 525–541.
[24] S. Zhao, T.M. Evans, X. Zhou, Effects of curvature-related DEM contact model on the macro-and micro-mechanical behaviours of granular soils, Géotechnique 68 (12) (2018) 1085–1098.
[25] C.M. Pereira, A.L. Ramalho, J.A. Ambrósio, A critical overview of internal and external cylinder contact force models, Nonlinear Dyn. 63 (4) (2011) 681–697.
[26] K.L. Johnson, One hundred years of Hertz contact, Proc. Inst. Mech.Eng. 196 (1) (1982) 363–378.
[27] M. Machado, P. Moreira, P. Flores, H.M. Lankarani, Compliant contact force models in multibody dynamics: evolution of the Hertz contact theory, Mech. Mach. Theory 53 (2012) 99–121.
[28] R.D. Mindlin, Compliance of elastic bodies in contact, J. Appl. Mech. ASME 16 (1949) 259–268.
[29] K. Kildashti, K. Dong, B. Samali, An accurate geometric contact force model for super-quadric particles, Comput. Methods Appl. Mech.Eng. 360 (2020) 112774.
[30] C. Cattaneo, Sul contatto di due corpi elasticie: distribution locale degli sforzi, Reconditi dell Academia Nazionale die Lincei 27 (1938) 474–478.
[31] H.-K. Kim, D.A. Hills, D. Nowell, Partial slip between contacting cylinders under transverse and axial shear, Int. J. Mech. Sci. 42 (2) (2000) 199–212.
[32] O.I. Zhupanska, A.F. Ulitko, Contact with friction of a rigid cylinder with an elastic half-space, J. Mech. Phys. Solids 53 (5) (2005) 975–999.
[33] T. Klimchuk, V. Ostryk, Stress distributions in the Cattaneo–Mindlin problem on a contact with slip and adhesion of two cylindrical bodies, Front. Mech. Eng. 6 (2020) 22.
[34] R.L. Burguete, E.A. Patterson, A photoelastic study of contact between a cylinder and a half-space, Exp. Mech. 37 (3) (1997) 314–323.
[35] C. Pereira, A. Ramalho, J. Ambrosio, Applicability domain of internal cylindrical contact force models, Mech. Mach. Theory 78 (2014) 141–157.
[36] J.M. Skotheim, L. Mahadevan, Soft lubrication: the elastohydrodynamics of nonconforming and conforming contacts, Phys. Fluids 17 (9) (2005) 092101.
[37] J. Blanco-Lorenzo, E.G. Santamaria, J. Vadillo, N. Correa, On the influence of conformity on wheel–rail rolling contact mechanics, Tribol. Int. 103 (2016) 647–667.
[38] H. Hertz, D.E. Jones, G.A. Schott, Miscellaneous Papers, Macmillan and Company, 1896.
[39] R. Balevičius, Z. Mróz, A finite sliding model of two identical spheres under displacement and force control – part I: static analysis, Acta Mech. 224 (8) (2013) 1659–1684.
[40] J. Rojek, Contact modeling in the discrete element method, in: Contact Modeling for Solids and Particles, Springer, 2018, pp. 177–228.
[41] M. Gonzalez, A.M. Cuitiño, A nonlocal contact formulation for confined granular systems, J. Mech. Phys. Solids 60 (2) (2012) 333–350.
[42] N. Brodu, J.A. Dijksman, R.P. Behringer, Multiple-contact discrete-element model for simulating dense granular media, Phys. Rev. E 91 (3) (2015) 032201.
[43] J. Rojek, A. Zubelewicz, N. Madan, S. Nosewicz, The discrete element method with deformable particles, Int. J. Numer. Methods Eng. 114 (8) (2018) 828–860.
[44] Structural contact modeling guidelines, 2020, (https://www.comsol.com/support/knowledgebase/1102). Accessed: 2020-03-15.
[45] R. Balevičius, Z. Mróz, Modeling of combined slip and finite sliding at spherical grain contacts, Granul. Matter 20 (1) (2018) 10.
[46] R. Balevičius, Z. Mróz, Relative transverse slip and sliding of two spherical grains in contact, J. Eng. Mech. 145 (4) (2019) 04019012.